

Cite this: *Mater. Adv.*, 2020,  
1, 2773

# Zinc-triggered photocatalytic selective synthesis of benzyl acetate on inverse spinel CuFe<sub>2</sub>O<sub>4</sub> 3D networks: a case of coupled redox photocatalytic reaction†

Yihan Zhang,<sup>‡</sup> Jingqi Tian,<sup>§</sup> Tengfei Jiang<sup>§\*</sup> and Huaiguo Xue

Coupled redox photocatalytic (CRP) reactions are a concept in which reduction and oxidation products are further reacted and serve as each other's redox partners. Herein, we developed a Zn-doped CuFe<sub>2</sub>O<sub>4</sub> 3D network for the CRP reaction to generate benzyl acetate with high selectivity. The ammonia assisted sol-gel method helps to improve the specific surface area of inverse spinel CuFe<sub>2</sub>O<sub>4</sub> and therefore the concentration of oxygen vacancies. With an optimized doping content of 0.5%, Zn-doped CuFe<sub>2</sub>O<sub>4</sub> presents a photocurrent as high as 34.72  $\mu\text{A cm}^{-2}$ , which indicates that Zn-doping largely boosts the charge separation efficiency in accordance with the surface photovoltage measurement. Most importantly, in the CRP reaction, zinc triggers the selectivity of benzaldehyde to benzyl acetate from 2.97% to 74.80%. Density functional theory (DFT) calculations further reveal that zinc doping enhances the adsorption energy of the intermediate product of acetone in CuFe<sub>2</sub>O<sub>4</sub>-based CRP reaction leading to enhanced activity and selectivity.

Received 8th July 2020,  
Accepted 28th August 2020

DOI: 10.1039/d0ma00486c

rsc.li/materials-advances

## Introduction

Heterogeneous photocatalysis plays an important role in solar energy conversion, such as solar water decomposition,<sup>1</sup> CO<sub>2</sub> reduction,<sup>2</sup> nitrogen fixation<sup>3,4</sup> and so on. So far, much work has focused on designing effective systems to collect and convert sunlight to meet high demand.<sup>5</sup> How to accelerate the basic process of charge separation is still a huge challenge, which is mainly impeded by the recombination on their way transferring to the (surface) active sites. The conventionally used sacrificial agents have been demonstrated to fully trap photoinduced electrons (or holes) to achieve so-called half reactions.<sup>6</sup> In previous work, molecular sacrificial agents such as formic acid,<sup>7</sup> ethanol,<sup>8</sup> glucose,<sup>9</sup> and dimethylamine<sup>10</sup> were used. Under these conditions, the photocatalysis is only at the expense of sacrificial agent consumption, which is a half-reaction rather than an overall photocatalysis.

Coupled redox photocatalytic (CRP) reactions are a concept in which corresponding reduction and oxidation products are further reacted and serve as each other's redox partners.<sup>11</sup> In this way, photocatalysis reactions occur with a small amount of

or even without using a sacrificial agent, which could enhance the charge separation efficiency and maximize the use of photo-induced charges. Recently, many reports focus on the CRP reaction.<sup>12,13</sup> Amer Hakki reported the synthesis of the corresponding N-alkylation compound *via* aniline coupled with aldehyde on TiO<sub>2</sub> nanoparticles with a yield of 90%,<sup>14</sup> in which the reactant aniline and aldehyde is generated from the photocatalytic reduction of nitroaromatic compounds and oxidation of solvent alcohol, respectively. Selvam Kaliyamoorthy reported the photocatalytic synthesis of the secondary amines *via* CRP reaction between aniline and aldehyde, which originates from the photocatalytic reduction of azobenzene, and photocatalytic oxidation of alcohols.<sup>15</sup> The proof-of-concept for CRP reactions are successfully confirmed by many other systems in addition to TiO<sub>2</sub>. Sarina prepared Au-Pd alloy catalysts for Suzuki-Miyaura cross-coupling, oxidative addition of benzylamine, selective oxidation of aromatic alcohols, and other organic syntheses driven by sunlight.<sup>16</sup> DaBin reported a novel, facile, and effective approach to the simultaneous production and functionalization of ultrathin 2D WO<sub>3</sub> nanosheets, and the as-prepared PdO@WO<sub>3</sub> nanohybrids exhibited excellent photocatalytic activity and recyclability in Suzuki cross-coupling reactions of various aryl halides under visible light irradiation.<sup>17</sup> WS<sub>2</sub> nanosheets,<sup>18</sup> carbon nitride,<sup>19</sup> microporous organic networks (MONs),<sup>20</sup> and layered double hydroxide (LDH)<sup>21</sup> are applied as photocatalysts in the oxidative coupling reactions of various amines. To the best of our knowledge, there is no investigation on inverse spinel CuFe<sub>2</sub>O<sub>4</sub> materials for CRP reactions. Therefore, it is urgent

School of Chemistry and Chemical Engineering, Yangzhou University,  
180 Siwangting Road, Yangzhou 225002, People's Republic of China.  
E-mail: jiangtengfei@yzu.edu.cn

† Electronic supplementary information (ESI) available. See DOI: 10.1039/d0ma00486c

‡ These authors contributed equally to this work.



to develop a suitable photocatalyst with a narrow band gap for CRP reactions.

Copper-based metal oxides are promising semiconductors with appropriate band energies for a variety of photocatalytic reactions. The spinel  $\text{CuFe}_2\text{O}_4$ , which is composed of non-toxic and inexpensive elements, has good light absorption and structural stability,<sup>22–25</sup> and can be used for carbon dioxide reduction and C–O/C–H bond activation.<sup>26,27</sup> However, their photocatalytic performance is largely inhibited by their poor ability for photogenerated charge separation. Additionally, their CRP applications have not been demonstrated yet.

Herein, zinc as a dopant in  $\text{CuFe}_2\text{O}_4$  is specified as a regulator to trigger the selectivity of benzaldehyde to benzyl acetate *via* CRP reaction, in which the photoinduced electrons and holes have been utilized simultaneously. The ammonia assisted sol-gel method helps to improve the specific surface area of  $\text{CuFe}_2\text{O}_4$  samples and the Zn dopant increases the concentration of oxygen vacancies, both of which are essential to improve the charge separation. Moreover, density functional theory (DFT) calculations have confirmed that zinc doping enhances the adsorption energy of the intermediate product of acetone in the  $\text{CuFe}_2\text{O}_4$ -based CRP reaction leading to enhanced activity and selectivity. This work provides a new idea for the acceleration of charge separation, lowering the expense of photocatalysis and generating a value-added product *via* the CRP reaction system.

## Preparation

### Synthesis of 3D Zn-doped $\text{CuFe}_2\text{O}_4$ networks

The  $\text{CuFe}_2\text{O}_4$  samples were synthesized by the ammonia-assisted sol-gel method. Typically, 5 mmol copper nitrate and 10 mmol iron nitrate with 0%, 0.3%, 0.5%, 1.0% and 1.5% (mole ratio) zinc nitrate were dissolved into tiny amounts of water. Then, 2.0 g of citric acid was added and stirred at room temperature for 5 minutes. Then, 6 mL of ammonia was added into the mixed precursor solution to generate the gel. The gel was dried at 70 °C for 5 hours and 130 °C for 7 hours. After sintering the dry gel at 500 °C under flowing air for 2 hours, the final products were obtained. Five samples were labeled as  $\text{CuFe}_2\text{O}_4$ ,  $\text{CuFe}_2\text{O}_4\text{-Zn}^{0.3}$ ,  $\text{CuFe}_2\text{O}_4\text{-Zn}^{0.5}$ ,  $\text{CuFe}_2\text{O}_4\text{-Zn}^{1.0}$  and  $\text{CuFe}_2\text{O}_4\text{-Zn}^{1.5}$ .

### Characterization

Scanning electron microscopy (SEM) images and energy-dispersive X-ray (EDX) elemental mapping images were obtained using a Zeiss-Supra55 electron microscope. High-resolution transmission electron microscopy (HRTEM) characterizations were performed using a Tecnai G2 F30 S-TWIN transmission electron microscope operated at 200 kV. X-ray diffraction (XRD) patterns of the products were recorded using a Bruker D8 Focus diffractometer by using Cu K $\alpha$  radiation ( $\lambda = 1.54178 \text{ \AA}$ ). UV-vis-NIR absorption spectra were recorded using a Cary 5000 UV-vis spectrometer. Raman spectroscopy was performed using a DXR2xi Micro Raman imaging spectrometer. XPS spectra were obtained using a ESCALAB 250Xi-Thermo Scientific X-ray photoelectron spectrometer. The Fourier transform infrared spectra (FTIR) were obtained using a TENSOR 27-Bruker spectrometer. Photoelectrochemical measurements were

performed in a three-electrode system. The  $\text{CuFe}_2\text{O}_4$  based work electrodes were fabricated using a dip-coating method. Typically, 1 mg of the  $\text{CuFe}_2\text{O}_4$  material was added in 4 mL of glycol methyl ether solution, and subjected to ultra-sound for 30 min. Then, the sample suspension was dropped onto the FTO substrate and heated at 80 °C. The electrode was sintered in a tube furnace at 400 °C for 30 min in air. The light source is a 500 W xenon lamp and the lamp power was adjusted to 100 mW  $\text{cm}^{-2}$ . The surface photovoltage (SPV) measurement was carried out on a home-made system based on the lock-in amplifier and the details of the system can be found in our previous work.<sup>28</sup> The stable adsorption configurations of acetone on  $\text{CuFe}_2\text{O}_4$  (001) was studied by DFT calculation with the CASTEP program. Every  $\text{CuFe}_2\text{O}_4$  slab had four atom layers where the top two layers were allowed to relax and the bottom two layers were frozen. Both structures were optimized at the generalized gradient approximation (GGA) level with Perdew–Burke–Ernzerhof (PBE) exchange–correlation functional and the ultra-soft pseudo-potentials. The vacuum layer of the interface models is set to be 10 Å to minimize the interaction between the periodic images. During the optimization, the lattice parameters were fixed and only the atoms were allowed to relax. The convergence threshold was set as  $2 \times 10^{-5} \text{ eV}$  in energy and 0.05 eV Å<sup>-1</sup> in force with a 351 eV plane-wave cutoff energy and a  $1 \times 1 \times 1$  *k*-point grid.

### Photocatalytic reaction

The catalyst (20 mg) was dispersed in 10 mL of isopropyl alcohol with 100 mmol benzaldehyde under a N<sub>2</sub> atmosphere. The light source is a 500 W xenon lamp. The conversions were determined by gas chromatography-mass spectrometry (GC-MS Agilent 7890B) based on benzaldehyde consumption.

## Results and discussion

The synthesis route of 3D Zn doped  $\text{CuFe}_2\text{O}_4$  networks is shown in Fig. 1. During the sol-gel process, ammonia is introduced, which plays the same role as the citric acid in terms of a complexing agent. Metal ions transform to complex compounds under the influence of citric acid and ammonia, which are uniformly dispersed over the solution. More importantly, ammonia provides a weak alkaline environment, which accelerates the hydrolysis rate during the heating process. Subsequently, the fast condensation between complex ions result in small agglomerates in the gel, which eventually crosslink to form a colloidal gel at 130 °C.<sup>29</sup> The gel decomposes to give a thoroughly mixed starting material consisting of a metal precursor for the following sintering at the temperature of 500 °C, which promotes necking formation between the  $\text{CuFe}_2\text{O}_4$  nanocrystals to generate a three-dimensional network structure. It is worth noting that the specific surface area of  $\text{CuFe}_2\text{O}_4\text{-Zn}^{0.5}$  is 23.74 m<sup>2</sup> g<sup>-1</sup>, which is double compared to that of  $\text{CuFe}_2\text{O}_4$  of 11.29 m<sup>2</sup> g<sup>-1</sup> (Fig. S1, ESI†). It is explained that for the doping element, zinc, has a strong affinity to form oxide clusters from the hydroxide precursor during the nucleation process.<sup>30</sup> The huge amounts of ZnO clusters act as seeds for particle growth, which results in the formation of a smaller particle size with a large specific surface area following LaMer's mechanism.<sup>31</sup>



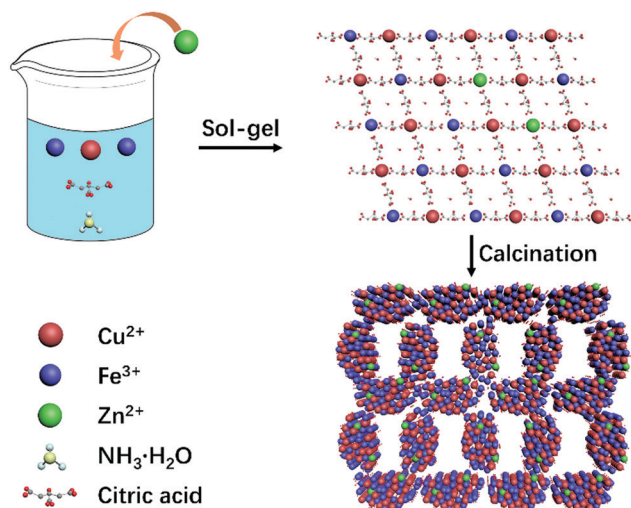


Fig. 1 The synthesis route of the 3D  $\text{CuFe}_2\text{O}_4$  and Zn doped  $\text{CuFe}_2\text{O}_4$  networks.

The morphology of typical samples was characterized by SEM and HRTEM (Fig. 2a, b, f and g). It is clearly observed that the samples exhibit a three-dimensional network structure consisting of cross-linked particles with a uniform size. The mean particle sizes are 100 and 65 nm for  $\text{CuFe}_2\text{O}_4$  and  $\text{CuFe}_2\text{O}_4\text{-Zn}^{0.5}$ , respectively. Through lattice analysis, two lattice fringes were found in the sample before doping, corresponding to the (2 0 2) and (1 0 1)

crystal planes, and two lattice fringes in the doped samples with the (0 0 4) and (1 0 3) crystal planes in accordance with the corresponding FFT diagrams (Fig. 2c-e, h-j). From the TEM images (Fig. 2b and g), it is observed that both the samples before and after doping consist of a uniform size of nanoparticles. HRTEM images and corresponding FFT diagrams show that  $\text{CuFe}_2\text{O}_4\text{-Zn}^{0.5}$  nanoparticles are highly crystalline. The SEM images of the  $\text{CuFe}_2\text{O}_4\text{-Zn}^{0.3}$ ,  $\text{CuFe}_2\text{O}_4\text{-Zn}^{1.0}$  and  $\text{CuFe}_2\text{O}_4\text{-Zn}^{1.5}$  samples are shown in Fig. S2 (ESI†). The atomic resolution high-angle annular dark-field scanning TEM (HAADF-STEM) image of the  $\text{CuFe}_2\text{O}_4$  and  $\text{CuFe}_2\text{O}_4\text{-Zn}^{0.5}$  nanoparticles (Fig. 1e and j) presents characteristic lattice spacings of 0.24 nm and 0.25 nm, which are attributed to the (0 2 2) and (1 1 2) lattice planes of  $\text{CuFe}_2\text{O}_4$ , respectively. In addition, the elemental mapping images of  $\text{CuFe}_2\text{O}_4\text{-Zn}^{0.5}$  supports the uniform distribution of Fe, Cu, O and Zn in the sample (Fig. 2l-p), which indicates that Zn atoms are doped in the whole crystal structure in accordance with EDS analysis (Fig. S3 and Table S1, ESI†). The doping atomic ratio of Zn has been measured by ICP to be 0.32%. The XRD patterns are shown in Fig. 2q to study the crystal structure of  $\text{CuFe}_2\text{O}_4$  oxides. The  $\text{CuFe}_2\text{O}_4\text{-Zn}^x$  sample is crystallized in an inverse spinel structure with a space group of  $I41/amd$ , in which half of the octahedral sites are occupied by  $\text{Cu}^{\text{II}}$  cations and the other half of the octahedral sites and all of the tetrahedral sites are occupied by  $\text{Fe}^{\text{III}}$  cations.<sup>32</sup> Rietveld refinement was performed to verify the structure of the samples as shown in Fig. S4 and Table S2 (ESI†). All these characteristics indicate

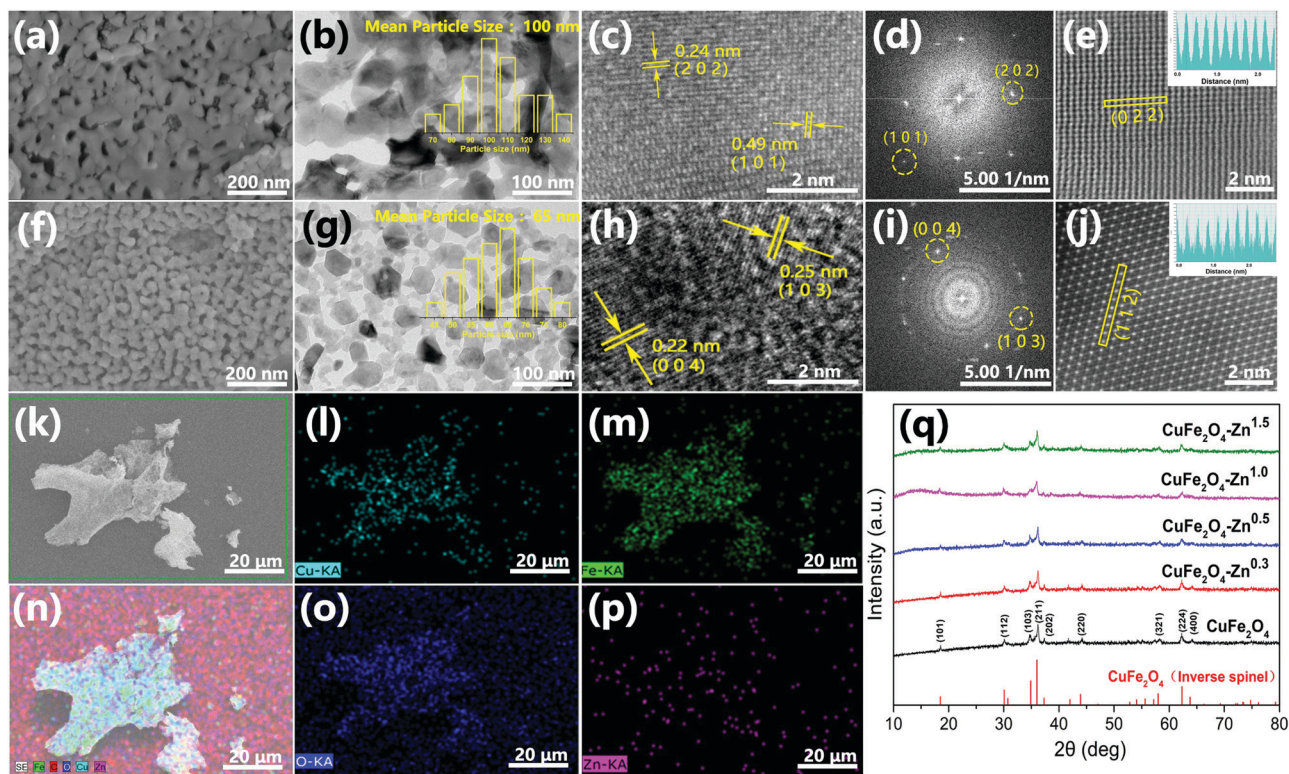


Fig. 2 SEM (a), TEM (b), HRTEM (c), corresponding FFT diagram (d), and atomic resolution HAADF-STEM image (e) of  $\text{CuFe}_2\text{O}_4$ ; SEM (f), TEM (g), HRTEM (h), corresponding FFT diagram (i), and atomic resolution HAADF-STEM image (j) of  $\text{CuFe}_2\text{O}_4\text{-Zn}^{0.5}$ ; the distribution maps of surface scanning elements Cu, Fe, O and Zn of EDS (k, l, m, n, o, p); the XRD spectra (q) of  $\text{CuFe}_2\text{O}_4$ ,  $\text{CuFe}_2\text{O}_4\text{-Zn}^{0.3}$ ,  $\text{CuFe}_2\text{O}_4\text{-Zn}^{0.5}$ ,  $\text{CuFe}_2\text{O}_4\text{-Zn}^{1.0}$  and  $\text{CuFe}_2\text{O}_4\text{-Zn}^{1.5}$ .





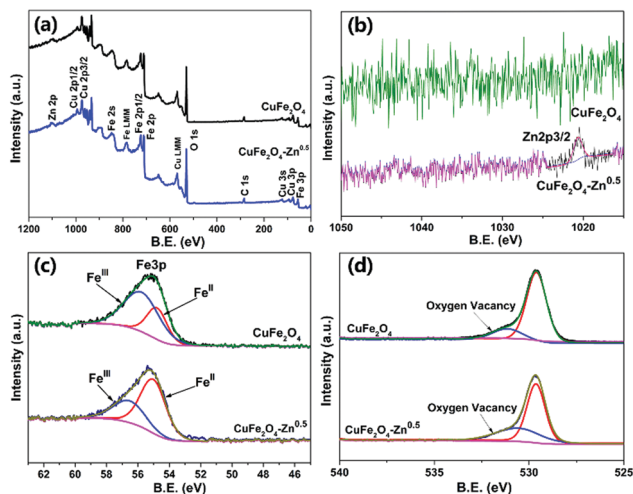


Fig. 3 XPS survey (a), Zn 2p (b), Fe 3p (c), and O 1s (d) spectra of pure  $\text{CuFe}_2\text{O}_4$  and  $\text{CuFe}_2\text{O}_4\text{-Zn}^{0.5}$ .

that Zn-doping does not change the crystal structure of inverse spinel  $\text{CuFe}_2\text{O}_4$ .

In order to further verify the composition of the prepared products, the binding energy of atoms on the surface of both  $\text{CuFe}_2\text{O}_4$  and  $\text{CuFe}_2\text{O}_4\text{-Zn}^{0.5}$  were studied by XPS. The presence of Cu, Fe and O can be clearly observed in the measured spectra (Fig. 3a). The characteristic peak of Zn proved that we have successfully prepared the zinc doped samples (Fig. 3b). The Fe 3p XPS peaks are shown in Fig. 3c, and the corresponding fitting results are shown in Table S3 (ESI<sup>†</sup>). It could be observed that the ratio of  $\text{Fe}^{\text{II}}/(\text{Fe}^{\text{II}} + \text{Fe}^{\text{III}})$  varies with the concentration of Zn with the maximum value of 71.76% for  $\text{CuFe}_2\text{O}_4\text{-Zn}^{0.5}$ . As shown in Fig. 3d, the O 1s core level peaks centered at 529.4 eV and 531.2 eV are attributed to the lattice oxygen and oxygen vacancy, respectively.<sup>33</sup> The ratio of oxygen vacancy is also changed with the ratio of  $\text{Fe}^{\text{II}}/(\text{Fe}^{\text{II}} + \text{Fe}^{\text{III}})$  (Fig. 3d), achieving the maximum value to 35.47% for  $\text{CuFe}_2\text{O}_4\text{-Zn}^{0.5}$ . According to the charge balance, the chemical formula of the sample is proposed as  $\text{CuZn}_x\text{Fe}_{2-y}^{\text{II}}\text{Fe}_y^{\text{III}}(\text{O}_{4-0.5x-0.5y})$ . So, when trivalent iron ions are substituted by divalent zinc, oxygen vacancies are generated, while the changes in XPS spectra of Cu 2p and Fe 2p are negligible as shown in Fig. S5 and S6 (ESI<sup>†</sup>).

The UV-vis-NIR absorption spectra present strong absorption of the  $\text{CuFe}_2\text{O}_4$  materials in the visible region (Fig. 4a). The change of the absorption intensity after Zn doping is insignificant. The optical band gaps of 2.31, and 2.39 eV are calculated for pure  $\text{CuFe}_2\text{O}_4$  and  $\text{CuFe}_2\text{O}_4\text{-Zn}^{0.5}$  from Tauc plots as shown in Fig. 4b. The Raman spectra in Fig. S7 (ESI<sup>†</sup>) show that two strong absorption peaks were found at  $480\text{ cm}^{-1}$  and  $690\text{ cm}^{-1}$ , which were consistent with the literature.<sup>34</sup> The FTIR spectra of the samples are shown in Fig. S8 (ESI<sup>†</sup>). It was proved that the materials did not contain any impurities and that trace zinc doping had little effect on their structure. To illustrate the effect of Zn doping on the charge separation process, the chopped  $I-t$  at  $-0.7\text{ V}$  was performed in  $1\text{ M NaOH}$  electrolyte as shown in Fig. 4c. The  $\text{CuFe}_2\text{O}_4$  electrodes show the photocathode current under an illumination of  $100\text{ mW cm}^{-2}$ , which present the

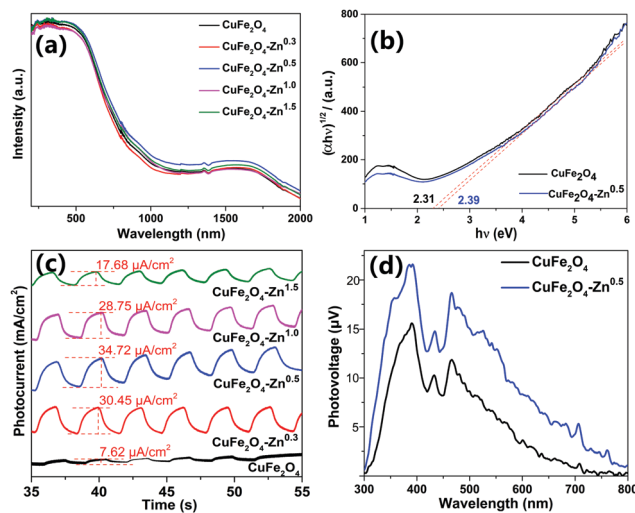
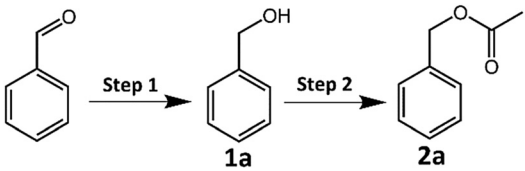


Fig. 4 The UV-vis-NIR spectra (a) of  $\text{CuFe}_2\text{O}_4$ ,  $\text{CuFe}_2\text{O}_4\text{-Zn}^{0.3}$ ,  $\text{CuFe}_2\text{O}_4\text{-Zn}^{0.5}$ ,  $\text{CuFe}_2\text{O}_4\text{-Zn}^{1.0}$  and  $\text{CuFe}_2\text{O}_4\text{-Zn}^{1.5}$ . The Tauc plots (b) of  $\text{CuFe}_2\text{O}_4$  and  $\text{CuFe}_2\text{O}_4\text{-Zn}^{0.5}$ . The  $I-t$  curves of  $\text{CuFe}_2\text{O}_4$ ,  $\text{CuFe}_2\text{O}_4\text{-Zn}^{0.3}$ ,  $\text{CuFe}_2\text{O}_4\text{-Zn}^{0.5}$ ,  $\text{CuFe}_2\text{O}_4\text{-Zn}^{1.0}$  and  $\text{CuFe}_2\text{O}_4\text{-Zn}^{1.5}$  (c), the SPV of  $\text{CuFe}_2\text{O}_4$  and  $\text{CuFe}_2\text{O}_4\text{-Zn}^{0.5}$  (d).

p-type property of  $\text{CuFe}_2\text{O}_4$ . The  $\text{CuFe}_2\text{O}_4\text{-Zn}^{0.5}$  presents the largest photocurrent of  $34.72\text{ }\mu\text{A cm}^{-2}$ , which is about five times that of the pure  $\text{CuFe}_2\text{O}_4$  sample. The enhancement of photocurrent could be ascribed to the efficient charge separation induced by zinc doping. While a large doping amount of zinc introduces impurity levels, which become recombination centers for photoinduced charge carriers and result in a weak photocurrent. To further illustrate the behavior of photoinduced charge carriers, the SPV measurement is carried out as shown in Fig. 4d. When the  $\text{CuFe}_2\text{O}_4$  sample is irradiated under incident light with a wavelength lower than  $800\text{ nm}$ , massive excess charge carriers are generated due to band-to-band transition and SPV signals arise when the charge was separated in spatial.<sup>35</sup> The maximum value of  $\text{CuFe}_2\text{O}_4\text{-Zn}^{0.5}$  is  $22\text{ }\mu\text{V}$  which is larger than that of  $\text{CuFe}_2\text{O}_4$  of  $16\text{ }\mu\text{V}$ . The SPV signal is proportional to the separated charge amount, so it could be inferred that the doping process increases the charge separation efficiency, which could generate a better photocatalytic performance. Linear sweep voltammetry (LSV) and the electrochemical impedance spectroscopy were also measured as shown in Fig. S9–S11 (ESI<sup>†</sup>).

The CRP reaction activity of the catalyst was investigated by converting benzyl alcohol (**1a**) to benzyl acetate (**2a**) in isopropanol solvent with a xenon lamp as a light source at  $62\text{ }^\circ\text{C}$  under a  $\text{N}_2$  atmosphere. All the reactions were completed in 2 hours, and the products were detected by GC-MS, and the GC-MS spectra of samples  $\text{CuFe}_2\text{O}_4$  and  $\text{CuFe}_2\text{O}_4\text{-Zn}^{0.5}$  are shown in Fig. S12 and S13 and in Tables S4 and S5 (ESI<sup>†</sup>). In the CRP reaction, a photogenerated electron ( $\text{e}^-$ ) reduces benzaldehyde to benzyl alcohol and a photogenerated hole ( $\text{h}^+$ ) oxidizes isopropanol to acetic acid, which the redox products react with each other to form benzyl acetate. The distribution of the products varies greatly for different  $\text{CuFe}_2\text{O}_4$  samples as shown in Table 1. It is clear that the selectivity is closely correlated to the doping amount of zinc in  $\text{CuFe}_2\text{O}_4$ . Benzyl alcohol (**1a**) was the main product for pure



**Table 1** Selective synthesis of benzyl acetate by CRP reaction for different CuFe<sub>2</sub>O<sub>4</sub> samples


| Entry | Catalyst  | <i>t</i> [h] | Conversion [%] | Selectivity [%] |       |
|-------|---|--------------|----------------|-----------------|-------|
|       |   |              |                | 1a              | 2a    |
| 1     | CuFe <sub>2</sub> O <sub>4</sub>                    | 2            | 92             | 95.58           | 2.97  |
| 2     | CuFe <sub>2</sub> O <sub>4</sub> -Zn <sup>0.3</sup> | 2            | 92             | 34.70           | 59.11 |
| 3     | CuFe <sub>2</sub> O <sub>4</sub> -Zn <sup>0.5</sup> | 2            | 92             | 15.86           | 74.80 |
| 4     | CuFe <sub>2</sub> O <sub>4</sub> -Zn <sup>1.0</sup> | 2            | 92             | 41.03           | 49.57 |
| 5     | CuFe <sub>2</sub> O <sub>4</sub> -Zn <sup>1.5</sup> | 2            | 92             | 38.32           | 51.63 |

CuFe<sub>2</sub>O<sub>4</sub>, and the yield was 95.58%. The selectivity of benzyl acetate (2a) was improved when increasing the zinc doping amount to 0.5%, and the highest selectivity was 74.80% for CuFe<sub>2</sub>O<sub>4</sub>-Zn<sup>0.5</sup>. It is explained that the CuFe<sub>2</sub>O<sub>4</sub>-Zn<sup>0.5</sup> sample has the highest charge separation efficiency and the photoinduced electrons accumulated at the particle surface reach the maximum, which present the best photocatalytic performance. The lifetime of the photoexcited electrons of the catalysts was measured *via* the open circuit photopotential decay method as shown in Fig. S14 (ESI<sup>†</sup>) and the lifetime was obtained by fitting the decay curve to an exponential function in Table S6 (ESI<sup>†</sup>). The CuFe<sub>2</sub>O<sub>4</sub>-Zn<sup>0.5</sup> exhibits the longest lifetime of the photoexcited electrons of 24.42 s, and more electrons are accumulated on the surface, which presents high charge separation efficiency and is good for catalytic reactions. A large amount of Zn changes the local chemical environment in CuFe<sub>2</sub>O<sub>4</sub> and therefore introduces impurity levels, which become recombination centers for photoexcited electrons. The band edge positions of the catalysts were measured using an electrochemical impedance spectroscopy method and the Mott-Schottky plots as shown in Fig. S15 (ESI<sup>†</sup>). The flat-band potential was determined from the *x*-intercept of the Mott-Schottky plots of reciprocal square capacitance *versus* potential. And the valence band edge is estimated by regarding the flat band potential as a reasonable approximation of the potential of the valence band edge.<sup>36</sup> So the valence band edges are 0.61 V, 0.53 V, 0.50 V, 0.56 V, and 0.56 V for CuFe<sub>2</sub>O<sub>4</sub>, CuFe<sub>2</sub>O<sub>4</sub>-Zn<sup>0.3</sup>, CuFe<sub>2</sub>O<sub>4</sub>-Zn<sup>0.5</sup>, CuFe<sub>2</sub>O<sub>4</sub>-Zn<sup>1.0</sup> and CuFe<sub>2</sub>O<sub>4</sub>-Zn<sup>1.5</sup>, respectively. For the CRP reaction, the oxidation and reduction work together and determine the photocatalytic performance. The selectivity depends on the separation of photoinduced holes and electrons rather than the valence band edge.

The comparative experiments were carried out, which show that both light and the photocatalyst are indispensable to drive the CRP conversion of benzaldehyde to benzyl acetate. We evaluated the photocatalytic activities of CuFe<sub>2</sub>O<sub>4</sub> and CuFe<sub>2</sub>O<sub>4</sub>-Zn<sup>0.5</sup> under various excitation wavelengths of 450 nm, 530 nm, and 625 nm from LED light sources. The results in Fig. S16 (ESI<sup>†</sup>) showed that the photocatalytic selectivity for benzyl acetate synthesis of CuFe<sub>2</sub>O<sub>4</sub> corresponded well with their optical absorption spectra. We carried out the recyclability of both CuFe<sub>2</sub>O<sub>4</sub> and CuFe<sub>2</sub>O<sub>4</sub>-

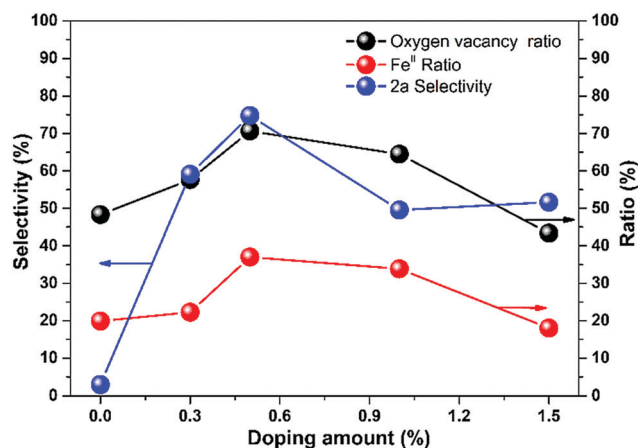
**Table 2** CRP reaction yields for different aldehydes and aromatic compounds by using the CuFe<sub>2</sub>O<sub>4</sub>-Zn<sup>0.5</sup> photocatalyst. (Isopropanol is used as the solvent, and the reaction time is 2 hours)

| Entry | Aldehydes aromatic compounds | Product | Yields [%] |
|-------|------------------------------|---------|------------|
| 1     |                              |         | 62         |
| 2     |                              |         | 68         |
| 3     |                              |         | 60         |
| 4     |                              |         | 54         |

Zn<sup>0.5</sup> samples in the photocatalytic selective synthesis of benzyl acetate as shown in Fig. S17 (ESI<sup>†</sup>), and measured the XPS and XRD of CuFe<sub>2</sub>O<sub>4</sub> and CuFe<sub>2</sub>O<sub>4</sub>-Zn<sup>0.5</sup> samples after the recycling test in Fig. S18–S20 (ESI<sup>†</sup>). The CuFe<sub>2</sub>O<sub>4</sub> and CuFe<sub>2</sub>O<sub>4</sub>-Zn<sup>0.5</sup> samples present good recyclability. There is no obvious change before and after the recycling test, which indicates the stability of both samples during the photocatalytic reaction.

The organic substrate for the CRP reaction is expanded to different aldehydes and aromatic compounds to explore the general applicability of the CuFe<sub>2</sub>O<sub>4</sub> photocatalysts as shown in Table 2. The CRP reaction is completely achievable and the yield is good. For example, the yields are 62%, 68%, 60%, and 54% for *p*-tolualdehyde, 3,5-dimethylbenzaldehyde, *m*-tolualdehyde, and 4-chlorobenzaldehyde.

To figure out the mechanism of the CRP performance, we plot the selectivity, oxygen vacancy ratio, and Fe<sup>II</sup> ratio over doping amount from the data in Tables 1 and 2. As shown in Fig. 5, the

**Fig. 5** The comparison of the ratio of oxygen vacancy, Fe<sup>II</sup> and selectivity of 2a with the change of doping amount.

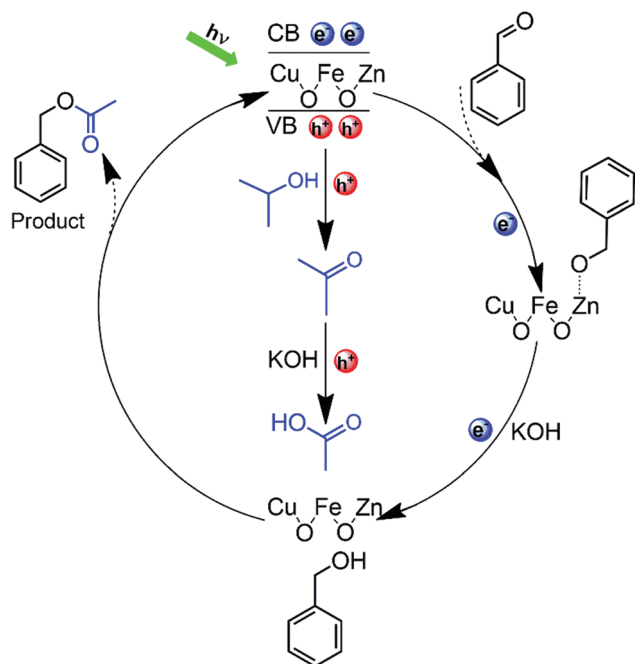


Fig. 6 The proposed mechanism for the CRP reaction of aldehydes to benzyl alcohol (**1a**) and further to benzyl acetate (**2a**) by Zn-doped CuFe<sub>2</sub>O<sub>4</sub>.

three values change with the doping amount and all of the maximum values located at 0.5% zinc doping amount of CuFe<sub>2</sub>O<sub>4</sub> of 35.47%, 71.76%, and 74.80% for selectivity, oxygen vacancy ratio, and Fe<sup>II</sup> ratio, respectively.

The possible reaction mechanism of the CRP reaction is proposed in Fig. 6. When the Zn-doped CuFe<sub>2</sub>O<sub>4</sub> material is irradiated by visible light ( $\lambda > 420$  nm), photoinduced electrons–holes pairs are generated. Immediately after, the photoinduced charge carriers are separated by the surface built-in electric field, which provides the possibility for further heterogeneous redox reaction. Initially, benzaldehyde undergoes one-electron reduction to generate the transition state species (Ar-CH<sub>2</sub>O•), after which, by the attack of another electron combined with proton, the (Ar-CH<sub>2</sub>O•) is reduced to benzyl alcohol. Simultaneously, isopropanol undergoes one-hole oxidation to acetone, with a following further oxidation by hydroxyl radicals to acetic acid, which are generated by hole oxidation. After then, the esterification reaction occurs between acetic acid and benzyl alcohol generating benzyl acetate as the final product. As shown in Table S7 (ESI), by using benzaldehyde and acetic acid as reactants, the selectivity of benzyl acetate is 70.55% (entry 1). Moreover, by using benzaldehyde and acetone as reactants and methanol as a scavenger, the benzyl acetate is detected (entry 2), which proves that the acetone is the very intermediate product. The competition reaction between methanol and benzaldehyde leads to the low selectivity of entry 2. It is known that the esterification reaction is easy to initiate, so the conversion of acetic acid from acetone is the rate-determining step, and the reasons are as follows: acetone is the very intermediate in the CRP reaction as discussed above; previous results reported that the isopropanol is easily converted to acetone by photocatalytic oxidation;<sup>37</sup> furthermore, acetone is more difficult to be further oxidized

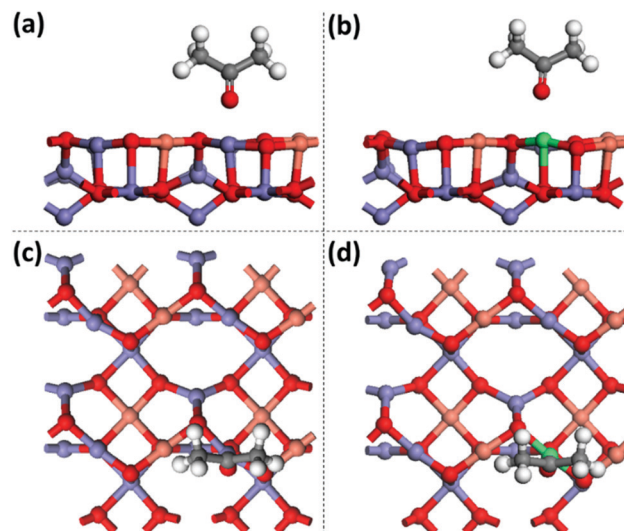


Fig. 7 Adsorption configurations of acetone on CuFe<sub>2</sub>O<sub>4</sub> (001) (a and c) and Zn-doped CuFe<sub>2</sub>O<sub>4</sub> (001) (b and d) with oxygen vacancy from DFT calculation.

than isopropanol, which can be proved from the electrochemical oxidation onset potential of  $-0.6$  V vs. NHE and  $-0.1$  V vs. NHE for isopropanol and acetone, respectively.<sup>38</sup> It is worth noting that the number of holes and electrons consumed in this CRP reaction are equal, which means that the organic reactants have the ideal conversion efficiency of 100% without any wasting of the sacrificial agent. In contrast, for pure CuFe<sub>2</sub>O<sub>4</sub>, the oxidation of isopropanol stays in acetone without further conversion, which results in low benzyl acetate selectivity. The above observations confirm that the Zn-doped CuFe<sub>2</sub>O<sub>4</sub> material could represent a valuable photocatalyst for the CRP reaction.

To understand the enhanced mechanism of the CRP reaction activity, the adsorption energy ( $E_{\text{ads}}$ ) of acetone was studied by DFT calculation with the CASTEP programs. The calculated adsorption configurations of acetone on the surface of CuFe<sub>2</sub>O<sub>4</sub> (001) are shown in Fig. 7, which presents that the O atom of acetone couples intimately with the Fe/Zn atom of CuFe<sub>2</sub>O<sub>4</sub>. Remarkably, the oxygen–metal bond lengths are extended from 2.075 Å for pure CuFe<sub>2</sub>O<sub>4</sub> to 2.309 Å for Zn-doped CuFe<sub>2</sub>O<sub>4</sub> with oxygen vacancy. Simultaneously, the  $E_{\text{ads}}$  of acetone shifts negatively from  $-0.61$  eV for CuFe<sub>2</sub>O<sub>4</sub> to  $-0.82$  eV for Zn-doped CuFe<sub>2</sub>O<sub>4</sub> with oxygen vacancy, which illustrates that the surface binding to acetone is more strong for Zn-doped CuFe<sub>2</sub>O<sub>4</sub> than that of CuFe<sub>2</sub>O<sub>4</sub> resulting in enhanced catalytic activity and selectivity. This explains the experimental observation in Table 1 that Zn-doped CuFe<sub>2</sub>O<sub>4</sub> has better benzyl acetate selectivity.

## Conclusions

A Zn-doped CuFe<sub>2</sub>O<sub>4</sub> 3D network was successfully prepared using an ammonia assisted sol–gel method with a large specific surface area, which was used for CRP reaction to selective synthesis of benzyl acetate. It is demonstrated that oxygen vacancies are generated when trivalent iron ions are substituted





by divalent zinc, which increases the charge separation efficiency. The DFT calculations reveal that the  $E_{\text{ads}}$  of acetone on the surface of Zn-doped  $\text{CuFe}_2\text{O}_4$  is larger than that of  $\text{CuFe}_2\text{O}_4$ . Consequently, the strongly adsorbed acetone suggested enhancing the conversion activity of acetone to acetic acid and therefore the high benzyl acetate selectivity. In our CRP reaction, the organic reactants exhibit the ideal conversion efficiency of 100% without wasting any of the sacrificial agent. This study provides a universal strategy for the design of the photocatalyst, which could inspire the further development of advanced spinel materials for CRP reactions with rational selectivity.

## Conflicts of interest

There are no conflicts to declare.

## Acknowledgements

The authors are grateful to the National Natural Science Foundation of China (Grant No. 21703201), the Natural Science Foundation of Jiangsu Province (Grant No. BK20170486), Postgraduate Research & Practice Innovation Program of Jiangsu Province (Grant No. XSJCX19\_065), the Priority Academic Program Development of Jiangsu Higher Education Institutions (PAPD), and Top-notch Academic Programs Project of Jiangsu Higher Education Institutions (TAPP) for their financial support.

## Notes and references

- 1 A. Fujishima, X. Zhang and D. A. Tryk, Heterogeneous photocatalysis: From water photolysis to applications in environmental cleanup, *Int. J. Hydrogen Energy*, 2007, **32**, 2664–2672.
- 2 X. Sun, C. Chen, S. Liu, S. Hong, Q. Zhu, Q. Qian, B. Han, J. Zhang and L. Zheng, Aqueous  $\text{CO}_2$  Reduction with High Efficiency Using  $\alpha\text{-Co}(\text{OH})_2$ -Supported Atomic Ir Electrocatalysts, *Angew. Chem., Int. Ed.*, 2019, **58**, 4669–4673.
- 3 J. Huang, B. Jin, H. Liu, X. Li, Q. Zhang, S. Chu, R. Peng and S. Chu, Controllable synthesis of flower-like  $\text{MoSe}_2$  3D microspheres for highly efficient visible-light photocatalytic degradation of nitro-aromatic explosives, *J. Mater. Chem. A*, 2018, **6**, 11424–11434.
- 4 X. Chen, N. Li, Z. Kong, W.-J. Ong and X. Zhao, Photocatalytic fixation of nitrogen to ammonia: state-of-the-art advancements and future prospects, *Mater. Horiz.*, 2018, **5**, 9–27.
- 5 A. Ibhadon and P. Fitzpatrick, Heterogeneous Photocatalysis: Recent Advances and Applications, *Catalysts*, 2013, **3**, 189–218.
- 6 M. Canterino, I. Di Somma, R. Marotta, R. Andreozzi and V. Caprio, Energy recovery in wastewater decontamination: Simultaneous photocatalytic oxidation of an organic substrate and electricity generation, *Water Res.*, 2009, **43**, 2710–2716.
- 7 M. Canterino, I. Di Somma, R. Marotta and R. Andreozzi, Kinetic investigation of  $\text{Cu}(\text{II})$  ions photoreduction in presence of titanium dioxide and formic acid, *Water Res.*, 2008, **42**, 4498–4506.
- 8 T. Sakata and T. Kawai, Heterogeneous photocatalytic production of hydrogen and methane from ethanol and water, *Chem. Phys. Lett.*, 1981, **80**, 341–344.
- 9 M. R. John, A. J. Furgala and A. F. Sammells, Hydrogen generation by photocatalytic oxidation of glucose by platinized n-titania powder, *J. Phys. Chem.*, 1983, **87**, 801–805.
- 10 S. Helali, E. Puzenat, N. Perol, M.-J. Safi and C. Guillard, Methylamine and dimethylamine photocatalytic degradation—Adsorption isotherms and kinetics, *Appl. Catal., A*, 2011, **402**, 201–207.
- 11 J. Z. Bloh and R. Marschall, Heterogeneous Photoredox Catalysis: Reactions, Materials, and Reaction Engineering, *Eur. J. Org. Chem.*, 2017, 2085–2094.
- 12 K. Selvam and M. Swaminathan, One-pot photocatalytic synthesis of quinaldines from nitroarenes with Au loaded  $\text{TiO}_2$  nanoparticles, *Catal. Commun.*, 2011, **12**, 389–393.
- 13 A. Hakki, R. Dillert and D. W. Bahnemann, Arenesulfonic Acid-Functionalized Mesoporous Silica Decorated with Titania: A Heterogeneous Catalyst for the One-Pot Photocatalytic Synthesis of Quinolines from Nitroaromatic Compounds and Alcohols, *ACS Catal.*, 2013, **3**, 565–572.
- 14 A. Hakki, R. Dillert and D. W. Bahnemann, Factors affecting the selectivity of the photocatalytic conversion of nitroaromatic compounds over  $\text{TiO}_2$  to valuable nitrogen-containing organic compounds, *Phys. Chem. Chem. Phys.*, 2013, **15**, 2992–3002.
- 15 K. Selvam, H. Sakamoto, Y. Shiraishi and T. Hirai, One-pot synthesis of secondary amines from alcohols and nitroarenes on  $\text{TiO}_2$  loaded with Pd nanoparticles under UV irradiation, *New J. Chem.*, 2015, **39**, 2467–2473.
- 16 S. Sarina, H. Zhu, E. Jaatinen, Q. Xiao, H. Liu, J. Jia, C. Chen and J. Zhao, *J. Am. Chem. Soc.*, 2013, **135**, 5793–5801.
- 17 D. Yim, F. Raza, J. H. Park, J.-H. Lee, H.-I. Kim, J.-K. Yang, I.-J. Hwang and J.-H. Kim, *ACS Appl. Mater. Interfaces*, 2019, **11**, 36960–36969.
- 18 F. Raza, J. H. Park, H. R. Lee, H. I. Kim and J. H. Kim, *ACS Catal.*, 2016, **6**.
- 19 F. Su, S. C. Mathew, L. Mhlmann, M. Antonietti, X. Wang and S. Blechert, *Angew. Chem., Int. Ed.*, 2011, **50**, 657–660.
- 20 N. Kang, J. H. Park, K. C. Ko, J. Chun, E. Kim, H. W. Shin, S. M. Lee, H. J. Kim, T. K. Ahn and J. Y. Lee, *Angew. Chem., Int. Ed.*, 2013, **52**, 6228–6232.
- 21 X. J. Yang, B. Chen, X. B. Li, L. Q. Zheng, L. Z. Wu and C. H. Tung, *Catal. Commun.*, 2014, **50**, 6664–6667.
- 22 R. K. Selvan, V. Krishnan, C. O. Augustin, H. Bertagnolli, C. S. Kim and A. Gedanken, Investigations on the Structural, Morphological, Electrical, and Magnetic Properties of  $\text{CuFe}_2\text{O}_4$ – $\text{NiO}$  Nanocomposites, *Chem. Mater.*, 2008, **20**, 429–439.
- 23 J. Yu, S. Zhuang, X. Xu, W. Zhu, B. Feng and J. Hu, Photo-generated electron reservoir in hetero-p–n  $\text{CuO}$ – $\text{ZnO}$  nanocomposite device for visible-light-driven photocatalytic reduction of aqueous  $\text{Cr}(\text{VI})$ , *J. Mater. Chem. A*, 2015, **3**, 1199–1207.
- 24 I. Sullivan, B. Zoellner and P. A. Maggard, Copper(I)-Based p-Type Oxides for Photoelectrochemical and Photovoltaic Solar Energy Conversion, *Chem. Mater.*, 2016, **28**, 5999–6016.



- 25 B. Zhao, Z. Shi and Y. Yuan, Transition-metal-catalyzed Chelation-assisted C–H Functionalization of Aromatic Substrates, *Chem. Rec.*, 2016, **16**, 886–896.
- 26 J. Rosen, G. S. Hutchings, Q. Lu, R. V. Forest, A. Moore and F. Jiao, Electrodeposited Zn Dendrites with Enhanced CO Selectivity for Electrocatalytic CO<sub>2</sub> Reduction, *ACS Catal.*, 2015, **5**, 4586–4591.
- 27 N. Enjamuri, S. Hassan, A. Auroux, J. K. Pandey and B. Chowdhury, Nobel metal free, oxidant free, solvent free catalytic transformation of alcohol to aldehyde over ZnO–CeO<sub>2</sub> mixed oxide catalyst., *Appl. Catal., A*, 2016, **523**, 21–30.
- 28 T. Jiang, T. Xie, W. Yang, L. Chen, H. Fan and D. Wang, Photoelectrochemical and Photovoltaic Properties of p–n Cu<sub>2</sub>O Homojunction Films and Their Photocatalytic Performance, *J. Phys. Chem. C*, 2013, **117**, 4619–4624.
- 29 A. E. Danks, S. R. Hall and Z. Schnepp, The evolution of ‘sol–gel’ chemistry as a technique for materials synthesis, *Mater. Horiz.*, 2016, **3**, 91–112.
- 30 B. Ludi and M. Niederberger, Zinc oxide nanoparticles: chemical mechanisms and classical and non-classical crystallization, *Dalton Trans.*, 2013, **42**, 12554–12568.
- 31 N. T. K. Thanh, N. Maclean and S. Mahiddine, Mechanisms of Nucleation and Growth of Nanoparticles in Solution, *Chem. Rev.*, 2014, **114**, 7610–7630.
- 32 X. T. Wang, T. Ouyang, L. Wang, J. H. Zhong, T. Ma and Z. Q. Liu, Redox-Inert Fe(<sup>3+</sup>) Ions in Octahedral Sites of Co–Fe Spinel Oxides with Enhanced Oxygen Catalytic Activity for Rechargeable Zinc–Air Batteries, *Angew. Chem., Int. Ed.*, 2019, **58**, 13291–13296.
- 33 J. Xu, X. Xiao, J. Zhang, J. Liu, J. Ni, H. Xue and H. Pang, Oxygen Vacancies Enhancing Electrocatalysis Performance of Porous Copper Oxide, *Part. Part. Syst. Charact.*, 2017, **34**, 1600420.
- 34 K. Verma, A. Kumar and D. Varshney, Curr. Effect of Zn and Mg doping on structural, dielectric and magnetic properties of tetragonal CuFe<sub>2</sub>O<sub>4</sub>, *Appl. Phys.*, 2013, **13**, 467–473.
- 35 T. Jiang, T. Xie, Y. Zhang, L. Chen, L. Peng, H. Li and D. Wang, Photoinduced charge transfer in ZnO/Cu<sub>2</sub>O heterostructure films studied by surface photovoltage technique., *Phys. Chem. Chem. Phys.*, 2010, **12**, 15476–15481.
- 36 J. Gu, A. Wuttig, J. W. Krizan, Y. Hu, Z. M. Detweiler, R. J. Cava and A. B. Bocarsly, *J. Phys. Chem. C*, 2013, **117**, 12415–12422.
- 37 H. Zhang, L. Dai, Y. Feng, Y. Xu, Y. Liu, G. Guo, H. Dai, C. Wang, C. Wang, H.-C. Hsi, H. Huang and J. Deng, *Appl. Catal., B*, 2020, **275**, 119011.
- 38 Y. Cheng, Y. Liu, D. Cao, G. Wang and Y. Gao, *J. Power Sources*, 2011, **196**, 3124–3128.

